DIPARTIMENTO ENERGIA, POLITECNICO DI TORINO

Thermal Hydraulic numerical analysis of Fusion superconducting magnet systems

Phd Dissertation Thesis

Akshat Kholia

May, 2013

Submitted in conformity with the requirements for the Degree of Doctor in Philosophy

To My Father and 3 Ladies in my life…..

ACKNOWLEDGEMENT

I hereby, express my profound gratitude towards my supervisors, Prof. Roberto Zanino and Dr. Laura Savoldi Richard, for their indispensable support, motivation and encouragement during this phase of my life. I really appreciate the support from Phani Kumar Domalapally & Roberto Bonifetto and must acknowledge the discussions that I relished having with you, about Physics and life. I also wish to express my greatest regards to my friends, with whom I had a very good time during my stay in Italy. Some of them are Ram Kumar, Sandeep Miryala and Emad Khan.

Last but not the least, I wish to express my sincere thanks and deep regards to two warrior ladies in my life, my mother and sister without whose support, I couldn't even dream of pursuing higher studies. To my Father, I always believe that you're there with me. I wish to thank all the people who made contributions in their own ways, for making things happen for me. And also to the good and bad experiences, without which, I wouldn't have learnt life.

I also wish to acknowledge the role of milady, Reetika, in my life, for the salvation you provided!

Table of Contents

Abstract iii

List of Figures iv

Nomenclature vi

Chapter I : Magnetic Confinement Fusion and Numerical Modeling of Superconducting Magnets 1

§1.1 MAGNETIC CONFINEMENT FUSION 2

§1.2 Superconducting Magnet System 3

§1.3 Importance of Thermal Hydraulics & Modeling 6

§1.4 REFERENCES 8

Chapter II: Cryogenic Circuit, Conductor & Coil Model 9

§ 2.1 Modeling of the Winding/Case cooling channels 9

§§ 2.1.1 Extension from Mithrandir → M&M 12

§ 2.2 Modeling of the structures 16

§ 2.3 EXTERNAL CIRCUIT 17

§2.4 COUPLING BETWEEN COMPONENTS [1] 19

§ 2.5 REMARKS 21

§ 2.6 REFERENCES 22

Chapter III: W7X Non Planar Coil cool-down validation 24

§ 3.1 GEOMETRICAL SPECIFICATIONS 26

§ 3.2 MODEL 28

§ 3.3 SIMULATION SETUP 31

§ 3.4 RESULTS 33

§ 3.5 CONCLUSIONS 38

§ 3.6 REFERENCES 39

Chapter IV :KSTAR AC losses analysis for PF1 coil 40

§ 4.1 INTRODUCTION 41

§ 4.2 EXPERIMENTAL DETAILS 43

§§ 4.2.1 KSTAR PF hydraulic circuit 43

§§ 4.2.2 KSTAR PF1 coils and conductor 43

§§ 4.2.3 Scenarios 45

§ 4.3 AC LOSSES 47

§§ 4.3.1 HYSTERESIS LOSSES 48

§§ 4.3.2 COUPLING LOSSES 50

§§ 4.3.3 EDDY CURRENT LOSSES 53

§§ 4.3.4 HYSTERESIS LOSSES IN THE FERROMAGNETIC JACKET MATERIAL 54

§ 4.4 EXPERIMENTAL TRACE OF THE AC LOSS 54

CAMPAIGN 54

§ 4.5 MODELING OF THE PF1L COIL 56

§§ 4.5.1 WINDING MODEL 57

§§ 4.5.2 CRYOGENIC CIRCUIT 60

§ 4.6 SIMULATION STRATEGY AND RESULTS 62

§§ 4.6.1 PHASE-I (Single current pulse) 62

§§ 4.6.2 PHASE-II (Series of Trapezoidal pulses) 65

§§§ 4.6.2.1 Calibration of nτ and inter-turn, inter-pancake thermal coupling 66

§§§ 4.6.2.2 Comparison with experimental data 68

§ 4.7 CONCLUSIONS 71

§ 4.8 REFERENCES 72

CHAPTER V : CONCLUSIONS AND PERSPECTIVES 74

§ 5.1 REFERENCES 76

Appendix A 77

Appendix B 82

Appendix C 88

ABSTRACT

In the present scenario, the International Thermonuclear Experimental Reactor (ITER) is in progress and efforts are being made to extend ITER to DEMOnstration Power plant (DEMO) with the purpose to harness the fusion energy for peaceful and constructive purposes. ITER uses the sueperconducting magnet systems for trapping and maneuvering plasma inside the giant tokamak machines. Superconductivity only entails under the critical conditions of temperature, magnetic field and current density. If any of these parameters surpass the critical value, the quench ensues in the cable. In the real system scenarios, electromagnetic, radiative & conductive loads are present, which may affect the performance of the machine. The magnet designer can change the parameters in terms of current and magnetic field to ensure that the critical conditions are met, but when it comes to temperature, it is really hard to locate the hot spot locations.To envisage such situations, it is essential to study thermal hydraulics and hence system code is needed for the whole superconducting magnet system. For such purposes, Cryogenic Circuit, Conductor and Coil code (4C) was built, imbibing the thermal hydraulic modeling of the cable in Conduit conductors (including strands) coupled with structures (which give support to the winding pack, wound by conductors) and an external cryogenic circuit.

During the thesis work, the pre-existing 4C code, was modeled for various coils with or without external cooling circuit as required. Henceforth, it was implemented against the wide range of transients, fast transients (~ few seconds) as well as slow transients (~ few days or weeks) to test the flexibility of the code in studying the wide range of physical phenomenon on different time scales. Eventually, the results were validated against the available experimental data to observe the precision of the model in 4C code. One of the analysis carried out during this dissertation included the cool down of one of the non planar coils (NPC) used in Wendelstein 7-X, which was an example of slow transient. In the domain of fast transients, an extensive analysis of AC losses in one of poloidal field (PF) coils with an external cooling circuit, was performed for Korean Superconducting Tokamak Advanced Research (KSTAR), functional fusion device.

LIST OF FIGURES

Figure 1.1: CICC for the ITER coil. 4
Figure 1.2: Iso-view of ITER coil system. 5
Figure 2.1:Conductors to be used for ITER CS with an exploded view without jacket. 10
Figure 2.2: Typical coil cross section modeled in FREEFEM++ 16
Figure 2.3: Circuit modeled in dymola represented here for KSTAR PF1 analysis. 18
Figure 3.1: W7-X non planar coil (NPC) (courtesy of Babcock Noell GmbH) 25
Figure 3.2: Sensor locations on the coil casing for NPC 26
Figure 3.3: Case cooling channels soldered using the copper stripes of about 1mm. 27
Figure 3.4: The interturn insulation width for NPC, in the between different pancakes 28
Figure 3.5: Coil Model for NPC, W7-X 29
Figure 3.6: Smoothed boundary conditions for the winding and case cooling channels 32
Figure 3.7: Cooling circuit of winding and casing with locations of selected sensors. 33
Figure 3.8: Evolution of common outlet He temperature: experimental as well as computed 34
Figure 3.9: Global mass flow rate evolution: experimental as well as computed 36
Figure 3.10: Evolution of maximum temperature difference between casing surface 37
Figure 3.11: Computed trajectory on the coil cross section of the maximum temperature location and 2D temperature distribution 37
Figure 4.1: Location of the PF coils around the central axis of the tokamak as well as CS. 41
Figure 4.2: Schematic view of the KSTAR PF coil cooling circuit 44
Figure 4.3: Schematic view of the cooling channels in KSTAR PF1 with sensor locations 44
Figure 4.4: Trapezoidal Current scenario for the phase I 45
Figure 4.5: Trapezoidal Current scenario during phase II 46
Figure 4.6: Current averaged Magnetic field distribution 46
Figure 4.7: Magnetization loop for NbTi 49
Figure 4.8: Flow of the coupling current in a twisted composite strand/wire 50
Figure 4.9: Experimental trace of thermal-hydraulic effect of the AC losses. 55
Figure 4.10: KSTAR CICC cross section and Detail of the PF1 winding 57

Figure 4.11: Friction factor versus Reynolds number. 58
Figure 4.12: Computed loss distribution of the different contributions to ac losses 59
Figure 4.13: Schematic view of KSTAR PF1L circuit model.. 60
Figure 4.14: Temperature at the outlet during the Phase I: Computed as well as experimental 63
Figure 4.15: 2D map of the temperature distribution for KSTAR PF1 64
Figure 4.16: nτ calibration for the Phase II of the KSTAR PF1 AC loss analysis 67
Figure 4.17: Calibration of thermal resistance multiplier (ITIP) on the TCUR02 in shot # 4595. 68
Figure 4.18: Computed vs. measured outlet He temperature evolution for all shots. 69
Figure 4.19: Computed and experimental helium inlet mass flow rate evolution. 69
Figure 4.20: Computed vs. measured inlet and outlet He pressure evolution 70
Figure 4.21: Computed vs. measured maximum temperature increase at the inlet 70

NOMENCLATURE

General

CICC	Cable in Conduit Conductor
ITER	International thermonuclear Experimental Reactor
KSTAR	Korea Superconducting Tokamak Advanced Research
W7X	Wendelestein 7-X
PFC	Poloidal Field coil
TFC	Toroidal Field Coil
CS	Central Solenoid
4C	Cryogenic Circuit, Conductor & Coil Model

Chapter II

V	Helium flow velocity (m/s)
p	Helium pressure (Pa)
T	Helium temperature (K)
Λ_V	Momentum source (N/m^3)
Λ_ρ	Mass source (kg/m^3 s)
Λ_e	Energy Source (W/m^3)
w	Helium Enthalpy (J/kg)
x	Coordinate along the axial direction of the i^{th} conductor, measured from helium inlet (m)
c_v	Helium specific heat at constant volume (J/kgK)
c	Helium velocity (m/s)
A	Helium Cross sectional area
$\bar{u}$	Unknown vector for single conductor
$\bar{\bar{l}}$	Coefficient matrix for single conductor
NODES	Number of nodes on each conductor
M&M	Multi Conductor Mithrandir code
NCOND	Number of Conductors
$\bar{U}$	Unknown vector for M&M
$\bar{\bar{L}}$	Coefficient matrix for M&M
$\bar{\bar{\bar{K}}}$	Coupling matrix for M&M
$k_{i\leftrightarrow j}$	Coupling flux in between i^{th} and j^{th} conductors for M&M
$S_{i\leftrightarrow j}$	Exchange perimeter between i^{th} and j^{th} conductor
$D_{i\leftrightarrow j}\left(x_1^i, x_2^j\right)$	Driving term for the coupling between x_1^i and x_2^j
$C_{i\leftrightarrow j}\left(x_1^i, x_2^j\right)$	Transport coefficient in the exchange between the two conductors
Ω_1	first type of coupling between conductors implemented in M&M
Ω_2	second type of coupling between conductors

	implemented in M&M
(dm/dt)	Mass flow rate (kg/s)
h	Convective heat transfer coefficient (W/m^2 K)
P	Wetted perimeter (m)
DAE	Differential algebraic equations
t	time

Subscripts

h	Subscript for hole
b	Subscript for bundle
St	Subscript for strand
Jk	Subscript for jacket

Chapter III

CCC	Case Cooling Channels
DL	Double layered wound conductor
f	Friction factor
$f_{smoot\ h}$	Friction factor for smooth circular tube
M_f	Friction factor multiplier for NPC, W7X
$R_{thermal}$	Thermal resistance (W/m^2 K)$^{-1}$
$k_{insulation}$	Thermal conductivity of the insulation (W/m K)
Δx	Thickness of the insulation (m)
h_{CC}	Heat transfer coefficient for Case cooling channels (W/m^2 K)
M_h	Heat transfer coefficient multiplier for NPC, W7X

Chapter IV

PF1L/U	Poloidal field number 1, Lower and upper coils
ITIP	Inter turn and inter pancake
SHe	Super critical Helium
$\vec{B}$	Magnetic field (A/m)
$\vec{E}$	Electric field (V/m)
Jc	Critical current density (A/m^2)
Q	Energy density (J/m^3)
M	Magnetization (A/m)
i = I_t/I_c	Current ratio between transport current (I_t) and critical current (I_c)
I_t	Transport current (A)
d_{eff}	Effective strand diameter
A_{non_cu}	Area of non copper part of the superconducting strand (m^2)
Q_{hyst}	Dissipation due to hysteresis losses (W/m)
λ_i	Filling factor at i^{th} stage of mulistaged superconducting CICC.
$\dot{B}$	Change in magnetic field (A/m s)
β	Geometrical filling factor for the subcable

$n\tau$	Coupling time constant (s)
R_c	Contact resistance (ohm)
D	Diameter of the sub cable (m)
τ_m	Current ramp up or ramp down time (s)
τ_{cp}	Coupling time constant (s)
Q_{cp}	Dissipation due to coupling losses (W/m)
A_{st}	Area of a superconducting strand (m^2)
R_{st}	Resistivity of the copper strand (ohm-m)
A_{Cu}	Area of the copper strands (m^2)
$B_\perp$	Perpendicular component of the magnetic field (A/m)
$Q_{eddy\perp}$	Dissipation due to the eddy current losses (W/m)
ρ_{ss}	Resistivity of the conduit material (ohm-m)
w_0 , h_0	Outer width of the conduit (m)
w_i , h_i	Inner width of the conduit (m)
T_{out}	Temperature at the outlet (K)
T_{in}	Temperature at the inlet (K)
(dm/dt)	Mass flow rate (kg/s)
TCUR	Temperature sensors
Re	Reynold's number
Δ	Change

Subscripts

Comp	Computed results
Exp	Experimental results
Opt	Optimum value

CHAPTER I
MAGNETIC CONFINEMENT FUSION AND NUMERICAL MODELING OF SUPERCONDUCTING MAGNETS

Sun revered as the "God" is the closest star to our earth and is worshipped in many civilizations. The enormous energy produced by the sun, drive the seasons, currents in the ocean, weather, climate and life. Everything is planned to perfection by the Universe and so is the size and dynamics of this very star which is just optimal to sustain life on earth

The primary source of energy for sun like any other stars is fusion of low atomic weight nuclei (in the case of Sun, Hydrogen) to generate tremendous amount of energy along with helium. All of this is made possible by the gravitational force which produces immense pressure and temperature at the core of the Sun. The temperature rises up to 15×10^6 K to sustain the nuclear fusion. Hence, the mass of sun makes ground for this immense gravitational pressure required to sustain fusion.

Massive Energy produced via fusion sets us to wonder, whether is it possible to have fusion on earth as an energy providing option to resolve the imminent problem of energy crisis.

REQUIREMENTS OF FUSION [1, 2]

In modern scenario where we are running out of conventional sources of energy, this new, environmentally sustainable form of energy is a heartening answer to the apprehensions cast over the existence of alternate sources of energy to meet the requirements of growing world population.

By 2050, an expected rise in global population from six billion to nine billion and ever rising standards of living are expected to boost the demand for energy at an exponential rate.

No single technology can cater to this demand. For each have its strengths and weaknesses. Therefore a mix of power sources will be needed to meet the challenges of energy

security, sustainable development and environmental protection. Future energy supply options may comprise of conventional fossil fuels, nuclear fission, fusion, and renewable energy sources.

At present, 80% of the developed world's energy comes from fossil fuels. Environmental problems – the greenhouse effect and the effects of acidic pollution – and diminishing fuel supplies indicates that reliance on coal, gas and oil are severely constrained.

Nuclear fission will continue to make a major contribution to electricity generation but its growth is subject to public and political acceptability. Moreover, fission requires the proper disposition of radio-active waste.

Other option is to harness the renewable resources, such as wind energy, thermo hydraulic power plants etc. However, supplies from renewable sources are reliant on environmental conditions, and the deteriorating quality of environment makes it hard to depend on these resources. Moreover renewable resources are difficult to harness and their storage is ridden with technological challenges. Hence, to provide constant base load electricity, predictable and non-varying sources of energy are needed. This means a short-term reliance on fossil fuels and fission must be supplemented with the addition of fusion power..

Fusion offers a secure, long-term source of supply, with important advantages. These include: no production of greenhouse gases from the fusion process; no long-lived radioactive waste (all waste will be recyclable within 100 years); inherent safety features; and almost unlimited fuel supplies. On current estimates, the cost of fusion-generated electricity is predicted to be broadly comparable to that obtained from fission, renewables and fossil fuels.

Fusion, therefore, could have a key role to play in the energy market of the future, with the potential to produce at least 20% of the world's electricity by 2100.

§1.1 MAGNETIC CONFINEMENT FUSION

Having understood the necessity of harnessing the energy due to fusion, the ways of doing so effectively must be closely examined. One of the answers is to replace the gravitational

field for confinement and fusion of the lighter nuclei in the Sun with the Magnetic Field on Earth!

The most promising device for this is the "*Tokamak*", a Russian word for a ring- shaped magnetic chamber. The tokamak is the most developed magnetic confinement system and provides the basis for the design of future fusion reactors that use this method. It was invented in the Soviet Union during the 1960s and soon adopted by researchers around the world.

The main tokamak components and functions are as follows[3]:

- The plasma is contained in a *vacuum vessel*. The vacuum is maintained by external pumps. The plasma is created by letting in a small puff of gas, which is then heated by driving a current through it.
- The hot plasma is contained by a *magnetic field* which keeps it away from the machine walls. The combination of two sets of magnetic coils – known as toroidal and poloidal field coils – creates a field in both vertical and horizontal directions, acting as a magnetic 'cage' to hold and shape the plasma.
- Large *power supplies* are used to generate the magnetic fields and plasma currents.
- *Plasma current* is induced by a transformer, with the central magnetic coil acting as the primary winding and the plasma as the secondary winding. The heating provided by the plasma current (known as Ohmic heating) supplies up to a third of the 100 million degrees Celsius temperature required to make fusion occur.
- Additional plasma heating is provided by *neutral beam injecti*on and radio frequency heating, which are beyond the scope of this thesis..

§1.2 SUPERCONDUCTING MAGNET SYSTEM

As mentioned in the previous section, for sustaining and maneuvering the plasma currents high magnetic fields are required. The only way to have such high magnetic fields is possible by cables made using superconducting materials mainly Cable in Conduit Conductors

(CICC). The use of such Cables have advantages in terms of thermal stability that it offers, due to the excellent heat transfer process attributed to the sufficient helium enthalpy to absorb the thermal loads [4-6]). At the same time, steady state heat removal is accomplished by limiting the hydraulic length and minimizing the pressure drop, which reduces the pump load of the external cryogenic circuit. ITER specially has introduced new kind of the CICC with the helical central channel, so that more helium enthalpy is available for the cable to avert the quench situation. The picture (figure 1.1) of which is shown below.

Figure 1.1: CICC for the ITER coils (CS and PF) [7].

The main components of the Magnet Coil system are as follows:

1). *Coil Systems:* The coil system (figure 1.2) generally has :

a) Toroidal Field Coils: The main purpose of the toroidal field coils is to confine the plasma in the torus after the initiation of the plasma has taken place. For the ITER, there are 18 TF coils each with the capability of producing the magnetic field of 11.8 T. The whole conductor is then imbibed in the radial plates to manifest the coil alsong with the radial plates to provide the structural support against the electromagnetic force load.

b) Poloidal Field Coils: The purpose of the Poloidal Field (PF) coils is to maintain the plasma shape and stability. The poloidal field pinches the plasma away from the wall. Also the magnetic field in the poloidal direction is induced by both the plasma as well as

by the PF magnets. For example, in the case of ITER, the poloidal field coil system consists of six horizontal coils located radially outside the TF magnet structure. The conductor used is the Nb3Sn cable in conduit having the central channel.

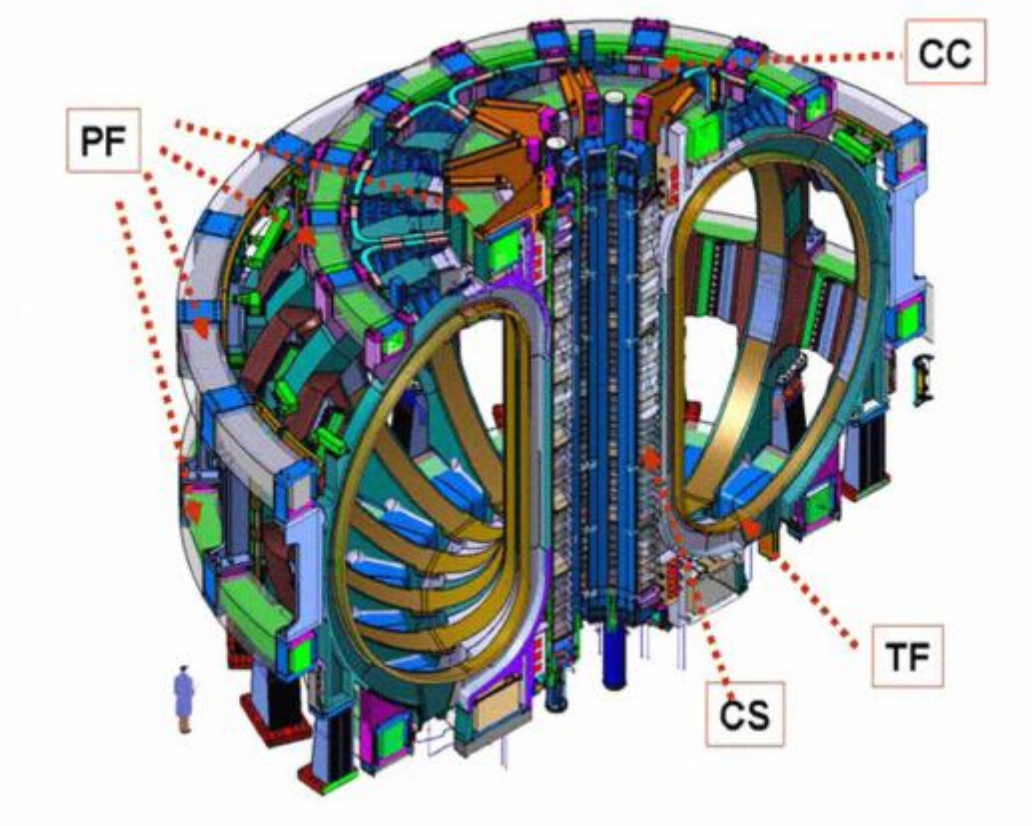

Figure 1.2: Iso-view of ITER coil system [7, 8].

c) Central Solenoid Coils: Central Solenoid (CS) coils, drives the plasma pulses by the law of the electromagnetic induction, during which the CS acts as a primary coil and the plasma acts as the secondary current loop. For ITER, the CS has six independent coil packs that use Nb_3Sn CICC superconducting conductor.

2). *Structures*: Supporting structures give the mechanical support to the coils against the electromagnetic force on the current carrying coil, so that it doesn't deform . The structures also have to be cooled to the temperature of the liquid helium to avoid the conduction from the structures to the superconductors leading to the abnormality in the functioning of the magnets. ITER for example has the SS (Stainless steel) radial plates to provide the mechanical support.

3). *Cryogenic System*: The dedicated Cryogenic System should always be present comprising of the Liquid Helium Plant, pumps, pipes and complete feeder circuit to feed the liquid helium to all the Coil systems, supporting structures, Cryostat and the vacuum vessels for keeping the whole magnet systems at low temperature (~ 4 K).

§1.3 IMPORTANCE OF THERMAL HYDRAULICS & MODELING

As we move towards the construction of the International Thermonuclear Experimental Reactor (ITER)[7], the availability of the numerical simulation codes for the thermal hydraulics assessment for the operating scenarios is of the utmost importance. This is due to the cost involved in building such big fusion machines and also because it is usually hard to locate the hot spot locations on the coil to extract the maximum performance out of it. The codes are usually referred as the "system codes" as they must include an adequate integrated description of several different sub-systems in the reactor, e.g. cryogenic system and the superconducting coil.

For this purpose, 4C code [8] was developed in Dipartimento Energia, Politecnico di Torino, which allowed to simulate the entire fusion grade magnet systems, in order to assess the hydraulic requirements of the actual system in actual situations. The 4C is an acronym for Cryogenic Circuit, Conductor and Coil, and hence incorporates a complete tool to model the whole magnet system right from the conductor level (meso-scale level) to Coil level on one hand and Cryogenic Circuit on the other.

During the present thesis, 4C code was used to perform the analysis of various transients scenarios envisaged by the fusion grade magnet coils during operation or tests.

The thesis analyzes the 4C code and uses it to model various coils, with or without the external cooling circuit, as per requirement. This was essential to ascertain the flexibility and reliability of the code against various transient scenarios. The results obtained through the analysis were validated against the experimental data provided, to guarantee the consistency of model used in 4C code. The transient may be slow (~ 1-2 weeks) or fast (~ few seconds) in nature. In the domain of slow transients, cool down test of one of the non planar coils (NPC) for Wendelstein 7-X stellarator was realized [9] (also see appendix A). However, in the domain of

fast transient, the comprehensive thermal hydraulic analsyis during the AC loss scenarios in one of poloidal field (PF1) coil used in Korean Superconducting Tokamak Advanced Research (KSTAR) were performed, with an external cooling circuit [10-12] (also see appendices B & C).

§1.4 REFERENCES

1. *http://www.ccfe.ac.uk/introduction.aspx*.
2. *https://en.wikipedia.org/wiki/Nuclear_fusion*.
3. *http://www.ccfe.ac.uk/Tokamak.aspx*.
4. V, A., *Thermodynamics of single-phase one-dimensional fluid.* Cryogenics, 1975, p. 285-289.
5. Wilson, M.N., *Superconducting Magnets*. 1983: Oxford University Press.
6. Iwasa, Y., *Case studies in Superconducting magnets: Design and operational issues*. 2nd ed. 2009: Springer.
7. Mitchell, N., et al., *The ITER magnet system.* IEEE Transactions on Applied Superconductivity, 2008. **18**(2): p. 435-440.
8. Savoldi Richard, L., et al., *The 4C code for the cryogenic circuit conductor and coil modeling in ITER.* Cryogenics, 2010. **50**(3): p. 167-176.
9. Bonifetto, R., et al., *Modeling of W7-X superconducting coil cool-down using the 4C code.* Fusion Engineering and Design, 2011. **86**(6-8): p. 1549-1552.
10. Savoldi Richard, L., et al., *4C code analysis of thermal–hydraulic transients in the KSTAR PF1 superconducting coil.* Cryogenics, 2013. **53**: p. 37-44.
11. Zanino, R., et al., *Simulation of Thermal–Hydraulic Transients in the KSTAR PF1 Coil Using the 4C Code.* IEEE Transactions on Plasma Science, 2012. **40**(3): p. 710-714.
12. *DYMOLA (Dynamic Modeling Laboratory) User's Manual, Version 5.3*. 2004, DYNASIM AB: Lund, Sweden.

CHAPTER II
CRYOGENIC CIRCUIT, CONDUCTOR & COIL MODEL

The comprehensive analysis of superconducting magnets requires the simulation of the whole coil along with the external interfacing components like cryogenic circuit. This encompasses the modeling of simultaneous simulation of several conductors as well as the supporting structures on one side, and the modeling of external cryogenic cooling circuit on the other side. For this purpose, A new tool – the 4C code – was developed [1], which allowed the thermal hydraulic simulation with particular reference to: (1) the winding made of the cable in conduit conductors (CICC), (2) the structures (radial plates and the case of the toroidal field – TF – Coils, for instance) and (3) the cooling circuits.

Each module of this model will be discussed elaborately in this chapter, with reference to the modeling of each component i.e. Windings/Conductor (CICC), Coils (which extends the modeling of winding to the supporting structures encapsulating winding pack) and the cryogenic cooling circuit (to feed helium to all components of the system). Henceforth, the coupling of each aforementioned module components will be discussed.

§ 2.1 MODELING OF THE WINDING/CASE COOLING CHANNELS

In the recent past, the development of the concept of the dual-channel CICC (figure 2.1) had led to the two fluid Mithrandir Code [2, 3]. The cross section of a dual channel conductor was modeled by Mithrandir accounting for: (1) Two fluid regions (hole and bundle) separated by a helical interface, (2) Superconducting strands, and (3) Jacket and insulation.

The ability for the code to work on the different time scales was attributed to the different thermodynamic conditions i.e. temperature and pressure of He in the hole and the bundle. Since the pressure waves travel with the speed of the sound, the pressure equalization occurs in the order of seconds, which is also the time scale of fast phenomenon like quench. However, the temperature equalization takes places depending on the mass flow rate and thermal conductivity

Figure 2.1:Conductors to be used for ITER CS [4]. The picture on the left shows the jacketed petal type cross-section of a condctor with a central channel. Picture on the right shows the exploded view of the conductor without jacket.

of the helium inside the bundle as well as in the hole. The time scale of which, is of the order of the inverse of the Mach number of the flow. In addition to two channeled conductors, the code also works well on the conductors without the central channel, for example, KSTAR [4], W7X [5] etc.

Observing that the typical size of the conductor is quite exponentially smaller than its length, hence the assumption of one dimensional treatment along the length of the conductor was made. The second important assumption made in the model was the ideal flow conditions, with the dissipation concentrated in the fanning friction factor viscosity.

With the aforementioned assumptions, the two fluids were separately modeled by a set of Euler equations [3], written in the primitive variables flow speed V, pressure p and temperature T, which could be derived from mass, momentum and energy balances and are given in equations (2.1-2.3).

$$\frac{\partial V}{\partial t} + V\frac{\partial V}{\partial x} + \frac{1}{\rho}\frac{\partial p}{\partial x} = \frac{1}{\rho}\left[\Lambda_V - v\Lambda_\rho\right] \tag{2.1}$$

$$\frac{\partial p}{\partial t} + \rho c^2 \frac{\partial V}{\partial x} + V \frac{\partial p}{\partial x} + \rho c^2 \frac{V}{A} \frac{\partial A}{\partial x} = \Phi \left[\Lambda_e - V \Lambda_V - \left(w - \frac{V^2}{2} - \frac{c^2}{\Phi} \right) \Lambda_\rho \right] \quad (2.2)$$

$$\frac{\partial T}{\partial t} + \Phi T \frac{\partial V}{\partial x} + V \frac{\partial T}{\partial x} + \Phi T \frac{V}{A} \frac{\partial A}{\partial x} = \frac{1}{\rho c_v} \left[\Lambda_e - V \Lambda_V - \left(w - \frac{V^2}{2} - \Phi c_v T \right) \Lambda_\rho \right] \quad (2.3)$$

Here A, is the flow cross section (with slow variation along the conductor explicitly accounted for [6]). The model solves simultaneously three equations, for each fluid (He in the cable bundle and He in the hole).

The convective coupling between the hole and bundle region through the perforated helical interface is driven by the pressure difference between these two regions. While, the conductive coupling is driven by the jacket temperature difference [7].

The strands and the jacket were separately modeled by the one-dimensional heat conduction equation, while neglecting the heat capacity and the thermal conduction along the helical interface. Also, the jacket and strands were thermally coupled with the helium, which in turn could be heated externally by the joule effect, in the situation of quenching in conductor. A uniform current distribution was assumed across the cross section of strands with the joule heating computed with the simple resistive model.

Linear finite element Galerkin method was used for the spatial discretization of the final set of equations, with optional upwind stabilization of the convective terms. An adaptive mesh had been used to follow the quench fronts.

Boundary conditions for the fluid equations were imposed following the theory of characteristics, while adiabatic conditions had been assumed at the conductor ends for strands and jackets [3]. The resulting set of equations is eventually solved at each time step by a banded-system solver, with a computational cost proportional to the number of unknowns.

The capability of the code had been accurately validated to envisage thermal hydraulic transients in a complex joint + conductor system [6].

However, the main limitation of the Mithrandir code as a predictive tool is that it allowed user to do the detailed analysis of only one conductor along with the hydraulic network

simulator, FLOWER [8, 9] and later DYMOLA. But the whole coil system, comprises of series of conductor connected electrically in series and hydraulically parallel. Also, the inter conductor coupling might not be negligible. This posed the limitation for the code.

§§ 2.1.1 EXTENSION FROM MITHRANDIR → M&M

The M&M code [7] had been developed from Mithrandir in order to realize many conductors comprising in the coil simultaneously. This tool allowed to model and simulates all the conductors in the coil, with or without the central channel. Each of the conductors was defined with the separate geometrical details including the material properties, magnetic field load and external heating load. The spatial discretization accounted for different adaptive meshes on different conductors. Also, the material properties such as thermodynamic properties of helium, insulation material, copper and superconductors were kept as a dynamical variable of temperature and pressure.

As mentioned above, the linear finite elements had been used for the spatial discretizaiton for Mithrandir. This resulted in a set of ordinary differential equations in time, linearized with frozen coefficient in time, lead to

$$\frac{d\bar{u}}{dt} = \bar{\bar{l}}\bar{u} \tag{2.4}$$

Where, $\bar{\bar{l}}$ is the coefficient matrix and vector $\bar{u}$ represents the unknowns. The column vector $\bar{u}$ is composed of 8 × NODES components, where NODES represent the number of nodes in the spatial mesh and 8 is the number of unknowns at each node. Hence for node n, the vector $\bar{u}$ one has [7],

$$\bar{u}\big((n-1)\times 8+1,\ldots.,n\times 8\big) = [V_h(n)\ V_b(n)\ p_h(n)\ p_b(n)\ T_h(n)\ T_b(n)\ T_{st}(n)\ T_{jk}(n)]^{-1} \tag{2.5}$$

Where $V(n)$, $p(n)$ and $T(n)$ are the hole (subscript h) and bundle (subscript b) computed values of flow speed, pressure and temperature, respectively, while $T_{st}(n)$ and $T_{jk}(n)$ are the computed values of strand and jacket temperature, respectively, always at node *n*.

For M&M, the system of equations extended to incorporate NCOND conductors. This changed the dimension of equation (2.4), which had now increased dimensions to simultaneously solve NCOND conductors. The length of the column vector increased to 8× NODES(NCOND)×

NCOND. Here, NODES is a function of NCOND because the number of nodes can be different for different conductors.

So, the set of equations solved in M&M was

$$\frac{d\bar{U}}{dt} = \bar{\bar{L}}\,\bar{U} + \bar{\bar{K}} \tag{2.6}$$

In equation (2.6), the unknown vector $\bar{U}$ was defined as

$$\bar{U} = \begin{bmatrix} \overline{u_1} \\ \overline{u_2} \\ \cdots \\ \overline{u_{NCOND}} \end{bmatrix} \tag{2.7}$$

As could be seen in the equation (2.7), it now took into account the u-vectors of single conductor Mithrandir code for all the conductors simultaneously, making a vector for the complete coil, i.e. $\bar{U}$. Also, extended from single conductor Mithrandir code to the M&M code was the coefficient matrix $\bar{\bar{l}}$, which transformed to $\bar{\bar{L}}$, for all the conductors in the coil. The coefficient matrix behaved as if there was no thermal coupling in between the conductors, which was explicitly defined inside the matrix $\bar{\bar{K}}$.

The coefficient matrix, $\bar{\bar{L}}$ hence took the following form:

$$\bar{\bar{L}} = \begin{bmatrix} \bar{\bar{l}}_1 & 0 & \cdots & 0 \\ 0 & \bar{\bar{l}}_2 & 0 & \vdots \\ \vdots & 0 & \ddots & 0 \\ 0 & \cdots & 0 & \bar{\bar{l}}_{NCOND} \end{bmatrix} \tag{2.8}$$

Here, $\bar{\bar{l}}_i$ is the coefficient matrix for the ith conductor, as in equation (2.4). The coupling matrix $\bar{\bar{K}}$ contained the off diagonal terms, accounting for the coupling of the different conductors, along the length of the conductor and the direction perpendicular to the flow of the liquid He (i.e. direction perpendicular to the length). The coupling terms were related to the temperature or pressure differences of the conductors depending on the type of coupling modeled in the code (see table 2.1)

Table 2.1: Coupled components and driving terms of di€erent kinds of coupling implemented in the M&M code, between the generic ith and jth conductors [7]

Coupling type	Exchanged property	Component involved in the coupling		$D_{i\leftrightarrow j}(x_i, x_j)$
		*i*th conductor	*j*th conductor	
Ω_1	Mass	He_B	He_B	Δp
	Momentum	He_B	He_B	Δp
	Energy	He_B	He_B	Δp
	Energy	He_B	He_B	ΔT
	Energy	He_B	Jacket	ΔT
Ω_2	Energy	Jacket	Jacket	ΔT

The form of coupling matrix $\overline{\overline{K}}$ was as follow:

$$\overline{\overline{K}} = \begin{bmatrix} 0 & K_{1\leftrightarrow 2} & \cdots & K_{1\leftrightarrow NCOND} \\ K_{2\leftrightarrow 1} & 0 & K_{2\leftrightarrow 3} & \cdots \\ \vdots & \cdots & 0 & K_{(NCOND-1)\leftrightarrow NCOND} \\ K_{NCOND\leftrightarrow 1} & \cdots & K_{NCOND\leftrightarrow (NCOND-1)} & 0 \end{bmatrix} \tag{2.9}$$

Where, the block $K_{i\leftrightarrow j}$ accounts for the coupling between the ith and jth conductor.

The equation (2.9), models the coupling along the length of conductor 1(say), with the corresponding coordinate along the length of conductor 2(say) and vice versa. Extending further the above mentioned point, the elements of block $K_{i\leftrightarrow j}$ were defined in terms of $k_{i\leftrightarrow j}\left(x_1^i, x_2^j\right)$, which gave the coupling fluxes between the point locate at position x_1 on the i^{th} conductor and the point located at position x_2 on the j^{th} conductor, with both coordinates measured from the respective conductors inlets.

The coupling flux, $k_{i\leftrightarrow j}\left(x_1^i, x_2^j\right)$ was defined as,

$$k_{i\leftrightarrow j}\left(x_1^i, x_2^j\right) = S_{i\leftrightarrow j}\left(x_1^i, x_2^j\right) \times D_{i\leftrightarrow j}\left(x_1^i, x_2^j\right) \times C_{i\leftrightarrow j}\left(x_1^i, x_2^j\right) \tag{2.10}$$

Where, $S_{i\leftrightarrow j}\left(x_1^i, x_2^j\right)$= Exchange perimeter between i^{th} and j^{th} conductor in the direction perpendicular to the flow.

$D_{i\leftrightarrow j}\left(x_1^i, x_2^j\right)$= Driving term for the coupling between x_1^i and x_2^j (see table 2.1)

$C_{i\leftrightarrow j}\left(x_1^i, x_2^j\right)$= Transport coefficient in the exchange between the two conductors, such as heat transfer coefficient.

The flexibility of the code lied in a fact that one could model different topologies for coupling between the conductors, both the "co-current" flow conductors (i.e. helium is flowing in the same direction in conductors) as well as the "Counter-current" flow conductors (i.e. helium flow is in opposite direction to each other in both conductors), by choosing the proper coordinates, x_1^i & x_2^j.

In general, all the couplings defined in equation (2.9), in the form of equation (2.10) could be implemented in the M&M code. The available choices of coupling are as follows:

1. *Coupling* Ω_1, including mass, momentum and energy exchanges. These were implemented with the rough valve model, as that used in Mithrandir for the hole-bundle coupling in a single two-channel conductor, as in [3]. This coupling could be used, such as, to simulate sub-channels or a single two-channel CICC.
2. *Coupling* Ω_2, including heat exchange between the jackets of adjacent conductors, driven by the temperature difference between the two solids. This accounted for the thermal resistance of the material interposed between the two jackets.

To compute the generic elements, $K_{i\leftrightarrow j}$ of the coupling matrix $\overline{\overline{K}}$, from the elements $k_{i\leftrightarrow j}\left(x_1^i, x_2^j\right)$, one needed to consider the corresponding axial co-ordinate to the spatial nodes of the i^{th} conductor. For each value of this co-ordinate, i.e. x_1^i, code determined the coupled co-ordinate i.e. x_2^j. This information is quite crucial, to allocate the proper location of the coupling term on the sub matrix $K_{i\leftrightarrow j}$ to form the coupling matrix.

The model (equation (2.6)) prepared in M&M also needed to be efficient computationally, in fact, similar to as the banded-system solver used in Mithrandir. This in turn was dependent on the choice of time discretization and majorly dependent on the explicit or implicit treatment of matrix $\overline{\overline{K}}$. The implicit treatment would anyway destroy the banded

structure of the matrix, leading to the increase in the computational cost and also the CPU time. On the contrary, the use of explicit treatment maintained the banded structure of the coefficient matrix and was adopted in M&M. Although the explicit treatment would be paid off by a typically lower maximum time step, than was affordable by an implicit method.

Actual coil comprises of the coil casing and also there is a presence of case cooling channels (shown in figure 2.2), which is present to have the same cooling as the winding pack itself. So, to have a complete picture of the coil, the case cooling channels were also modeled with the aforementioned strategy. The model solved 1D compressible (Euler like) flow equations in each channel, coupled to the 1D transient heat conduction along the cooling pipe through a Dittus-Boelter heat transfer coefficient. The case cooling channels were coupled to the structures (explained below) using the Robin type boundary condition [1].

§ 2.2 MODELING OF THE STRUCTURES

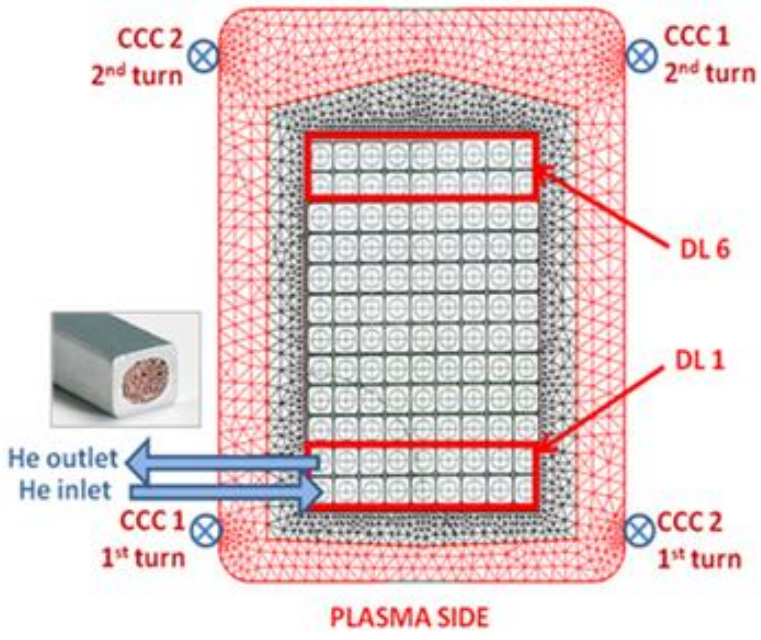

Figure 2.2: Picture shows the typical coil cross section modeled in FREEFEM++, the inner rectangular portion is the winding pack, which is embedded inside the coil casing. The coil casing is shown as the black and red meshes.

To model the coil completely, one must take into account the coupling of the conductors/winding pack with the external structures i.e. the coil case and radial plates, which provides the mechanical support to the coil against the electromagnetic load. The modeling of structures was also important due to the fact that due to the massive structures, they don't have the non negligible specific heat and had to be accounted for, in the model. Also, they are subjected to the heat load of neutrons and the eddy currents, which can be crucial input during the study of the transient.

The modeling of the structures was done by implementing the strategy of solving heat conduction equation on the 2D cuts, which were present along the poloidal direction of the coil. This strategy provided the complete 3D like (actually 2 ½ D) modeling of the coil [1]. The number of cuts depended on the transient times of the conduction along the poloidal direction and the convection-advection transient time. If the conduction time was slower as compared to the convection-advection time then there was a need of lesser 2D cross sections for convergent solution and vice versa.

This 2 ½ D heat conduction module was realized by using the public software FreeFem++ [10], for the radial plates (in the case of ITER TF coil) / coil casing.

Freefem++ has the ability to solve the partial differential equation of a given weak form using the Finite Element Method (FEM). This C++ based software, allows user to discretize the geometry in the triangular meshes based on the Delaunay-Voronoi algorithm; with the inner point density proportional to the density of points on the boundaries [11, 12].

§ 2.3 EXTERNAL CIRCUIT

4C code, comprises the modeling of the external cryogenic circuit needed to feed liquid helium to coils. The External circuit actually allows one to look at the complete picture of the various components of the circuit e.g. pump, pipes, valves etc, during the case of transients. This feature also allows to perform the predictive studies in the terms of pump requirements to curb the heat from the coils during the various load conditions [13].

Cryogenics 53 (2013) 37–44

Contents lists available at SciVerse ScienceDirect

Cryogenics

journal homepage: www.elsevier.com/locate/cryogenics

4C code analysis of thermal–hydraulic transients in the KSTAR PF1 superconducting coil

L. Savoldi Richard [a], R. Bonifetto [a], Y. Chu [b], A. Kholia [a], S.H. Park [b], H.J. Lee [b], R. Zanino [a,*]

[a] Dipartimento di Energetica, Politecnico di Torino, Torino 10129, Italy
[b] National Fusion Research Institute, Daejeon, Republic of Korea

ARTICLE INFO

Article history:
Available online 23 May 2012

Keywords:
Nuclear fusion
Superconducting coils
Thermal–hydraulic modeling
AC losses
KSTAR

ABSTRACT

The KSTAR tokamak, in operation since 2008 at the National Fusion Research Institute in Korea, is equipped with a full superconducting magnet system including the central solenoid (CS), which is made of four symmetric pairs of coils PF1L/U–PF4L/U. Each of the CS coils is pancake wound using Nb_3Sn cable-in-conduit conductors with a square Incoloy jacket. The coils are cooled with supercritical He in forced circulation at nominal 4.5 K and 5.5 bar inlet conditions. During different test campaigns the measured temperature increase due to AC losses turned out to be higher than expected, which motivates the present study.

The 4C code, already validated against and applied to different types of thermal–hydraulic transients in different superconducting coils, is applied here to the thermal–hydraulic analysis of a full set of trapezoidal current pulses in the PF1 coils, with different ramp rates. We find the value of the coupling time constant $n\tau$ that best fits, at each current ramp rate, the temperature increase up to the end of the heating at the coil outlet. The agreement between computed results and the whole set of measured data, including temperatures, pressures and mass flow rates, is then shown to be very good both at the inlet and at the outlet of the coil. The $n\tau$ values needed to explain the experimental results decrease at increasing current ramp rates, consistently with the results found in the literature.

© 2012 Elsevier Ltd. All rights reserved.

1. Introduction

The KSTAR tokamak [1] is operating since 2008 at the National Fusion Research Institute in Korea. KSTAR is equipped with a full superconducting magnet system, see Fig. 1a, including the central solenoid (CS), which is made of four symmetric pairs of coils PF1L/U–PF4L/U, see Fig. 1b. Each of the CS coils is pancake wound using cable-in-conduit conductors with a square Incoloy 908 jacket containing a multi-stage cable made of 240 Nb_3Sn and 120 Cu strands. The coils are cooled with supercritical He in forced circulation at nominal 4.5 K and 5.5 bar inlet conditions. In the different KSTAR campaigns, a higher temperature rise than expected [2] was observed in the PF1L/U coils during pulsed current operation [3]. This effect could in principle have a severe influence on the future plasma operation, limiting the current changing rates. It then becomes important to have a model which can adequately simulate the results from the KSTAR campaigns, so that the CS operation can be foreseen in the future. Clearly, an accurate thermal–hydraulic simulation tool is necessary to achieve this goal.

The Cryogenic Circuit Conductor and Coil (4C) code [4] was already validated against different types of thermal–hydraulic (TH) transients in different superconducting coils and cryogenic circuit, including the cool-down of a W7-X non-planar coil [5], the safety discharge of the ITER Toroidal Field Model Coil [6,7], the dynamic modeling of a saturated He bath subjected to pulsed heat load [8,9]. Among other applications [10–13], the 4C code was also recently applied (with a simplified model of the external cryogenic circuit) to the analysis of AC losses in the PF1L/U coils [14], confirming the inconsistency between the expected and measured maximum temperature rise in the winding and highlighting the possible underestimation of the coupling time constant $n\tau$.

Here we study with the 4C code a full set of current trapezoidal pulses with different ramp rates in the PF1L/U coils, performed during the 2011 experimental campaign [15]. We model a single PF1 coil (PF1L), accounting for coupling losses in the SC strands, eddy current losses in the pure copper strands and in the jacket, as well as hysteresis losses in the superconducting filaments. In view of the uncertainties in the actual value of the coupling time constant $n\tau$ in the PF1 conductors, we find the $n\tau$ that allows best-fitting the outlet coil temperature signals during the current pulse, at each

* Corresponding author. Address: Dipartimento di Energetica, Politecnico di Torino, Corso Duca degli Abruzzi 24, Torino 10129, Italy. Tel.: +39 011 0904490; fax: +39 011 0904499.
E-mail address: roberto.zanino@polito.it (R. Zanino).

0011-2275/$ - see front matter © 2012 Elsevier Ltd. All rights reserved.
http://dx.doi.org/10.1016/j.cryogenics.2012.04.015

Nomenclature

dm/dt	helium mass flow rate (kg/s)
ITIP	inter turn/inter pancake
$n\tau$	coupling losses time constant
p	helium pressure (Pa)
PF	poloidal field
SC	superconductor
t	time (s)
T	helium temperature (K)
TCUR	temperature sensor

Greek

Δ	difference

Subscripts

comp	computed
exp	experimental
opt	optimum
out	coil outlet

Superscripts

max	maximum

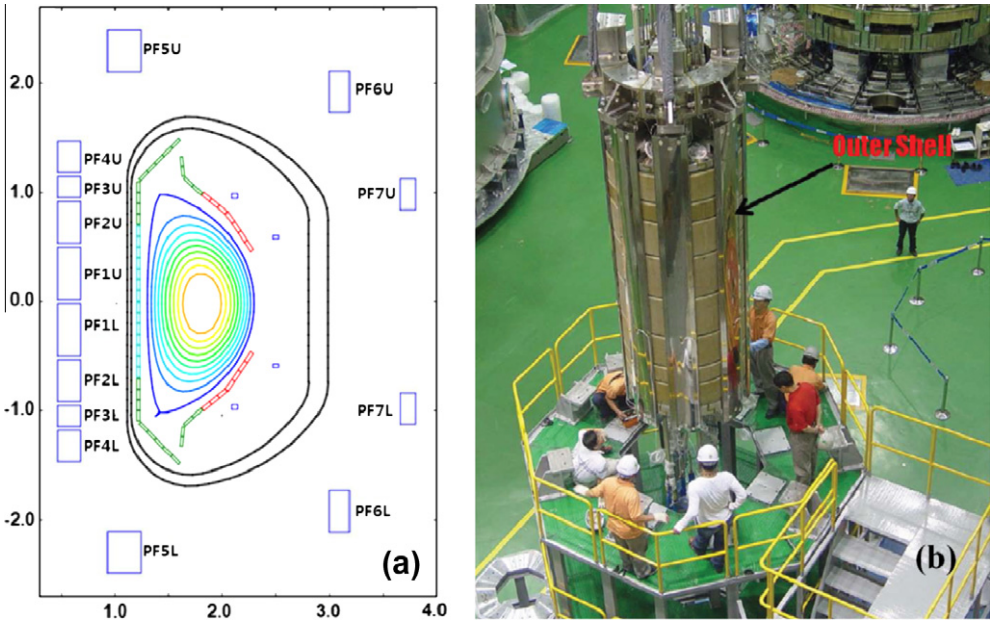

Fig. 1. (a) Poloidal cross section of the KSTAR vacuum vessel and superconducting PF coils. (b) The KSTAR central solenoid.

different current ramp rate. We also calibrate the thermal diffusion that takes place between adjacent turns and pancakes inside the coil. Eventually we compare the computed inlet/outlet temperature and pressure and the inlet mass flow rate with the corresponding measured data, to assess the quality of the simulations.

2. Experimental setup

2.1. KSTAR PF hydraulic circuit

The cryogenic circuit that supplies He to the PF coils is sketched in Fig. 2: each PFU coil is connected in parallel with its PFL coil, with pressure sensor, thermometer and flow meter (Venturi) located on the common inlet pipe. All U/L pairs are connected in parallel to a single He distribution system. Additional diagnostics are present at a more local level, with a common inlet temperature sensor for the 10 channels of each PF1 coil, and with outlet temperature sensors for chan1, chan10 and for central channels grouped in pairs, see Fig. 3.

2.2. KSTAR PF1 coils and conductor

Each PF1 coil is pancake-wound using a single conductor. The PF1 conductor is a cable-in-conduit with a square Incoloy 908 jacket containing a multi-stage cable made of 240 Nb_3Sn and 120 Cu strands, see the inset in Fig. 3 and Table 1 for details. The cooling of the superconducting strands is guaranteed by five separate inlets located at the transition between adjacent double pancakes, see Fig. 3, where the inlets are located in the bore of the coil. As a result, the cooling path of each coil consists of 10 channels (double pancakes), hydraulically in parallel. The adjacent turns of any given pancake, as well as of adjacent pancakes, are separated by a multilayer turn insulation (2 kapton layers of 0.05 mm thickness, and 4 S-glass layers of ~0.18 mm thickness), see the inset in Fig. 3, which still allows thermal coupling/diffusion inside the coil. The two PF1 coils are completely symmetric, and they are fed in parallel by the same power supply.

2.3. Scenarios

Since the behavior of the two PF1 coils is very similar when subjected to a current pulse, see also [14], we restrict here the analysis to the PF1L coil. We consider five different AC loss tests with trapezoidal current pulses, performed in the 2011 test campaign [15]. For all shots the current ramp-up rate is equal to 1 kA/s, while the ramp-down rates are different (0.5 kA/s for shot # 4594, 1 kA/s for shot # 4595, 2 kA/s for shot # 4596, 4 kA/s for shot # 4597 and 6 kA/s for shot # 4598, respectively), see Fig. 4.

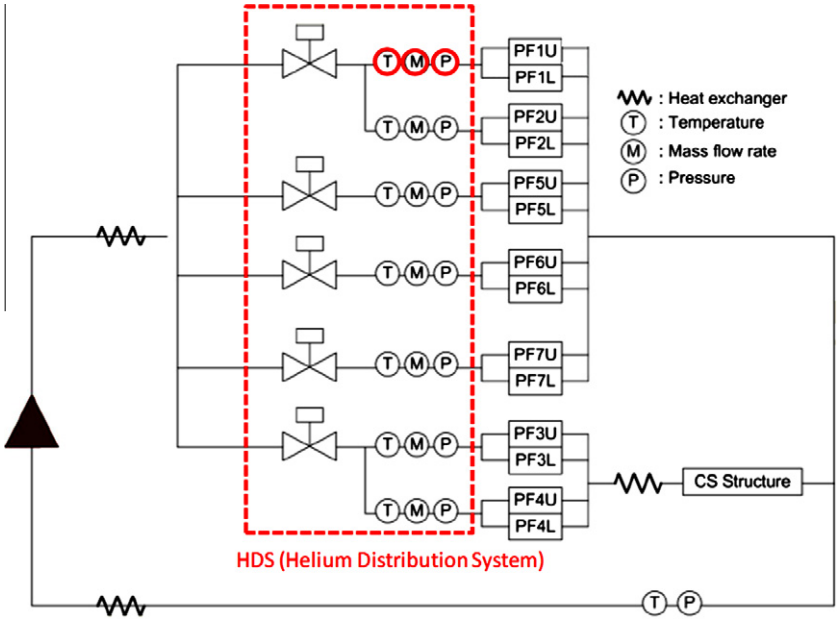

Fig. 2. Schematic view of the KSTAR PF coil cooling circuit.

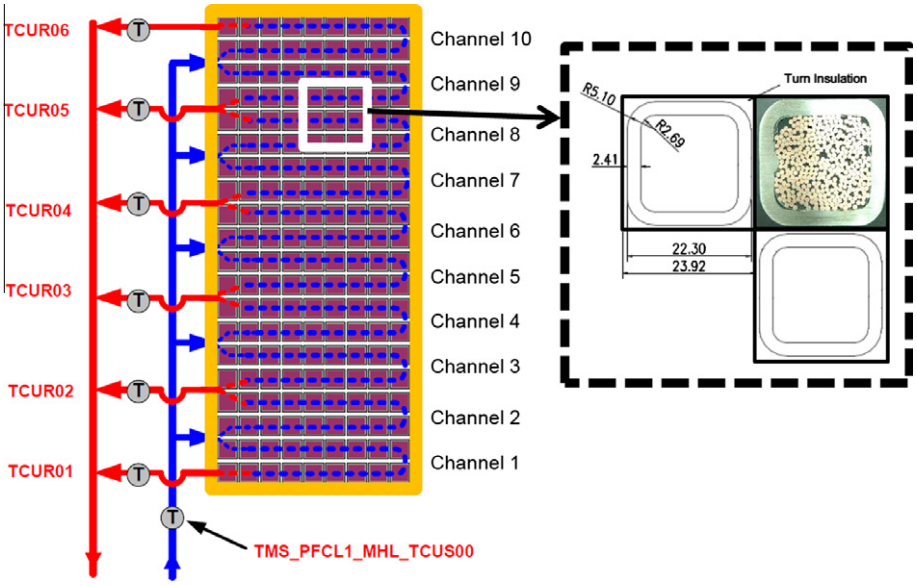

Fig. 3. Schematic view of the 10 parallel cooling channels in the PF1L coil and thermometers. Inset: conductor cross section.

Table 1
PF1 conductor parameters.

Superconductor	Nb_3Sn
Cable pattern	$3 \times 4 \times 5 \times 6$
SC/Cu strands	240/120
Strand diameter (mm)	0.78
Conduit material	Incoloy 908
Void fraction (%)	32.7
Channel hydraulic length (m)	64.5

The magnetic field distribution along the different channels (reference coordinate starting from the He inlet), due to the self-field and to the field of the PF1U coil, is reported in Fig. 5 for unit current, showing that the maximum field is achieved on the inner-most turns at the inlet and outlet of each channel, with slightly higher peak in the central channels. Concerning the side channels, the peak in channel 10 is higher than in channel 1 because of the closer proximity of channel 10 to the PF1U coil.

The measured response of the coil to the current pulse is shown in Fig. 6 for the two shots # 4595 (slow ramp-down) and # 4598 (fast ramp-down), respectively, in terms of inlet and outlet temperature evolutions. The two "side" temperature traces, corresponding to the outlet temperature of chan1 and chan10, see Fig. 2, are not reported, since at the two ends the conductor is jointed to the feeders and heat transfer occurs between the two, introducing some perturbation of the measured temperature trace. Both shots in Fig. 6 show a similar dynamics at the outlet: a first temperature increase, corresponding to the current ramp-up, ending with a short plateau, followed by a second increase up to the absolute maximum, corresponding to the current ramp-down. The increase up to the absolute maximum occurs on the current

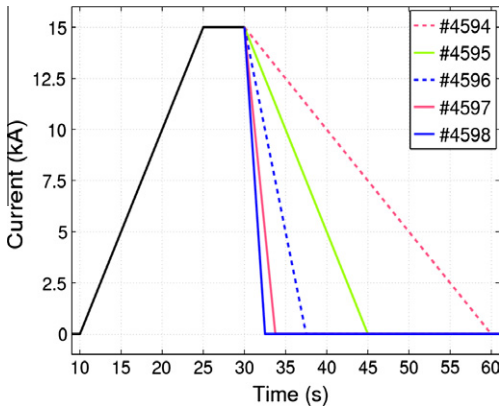

Fig. 4. Trapezoidal AC loss scenarios analyzed in this paper.

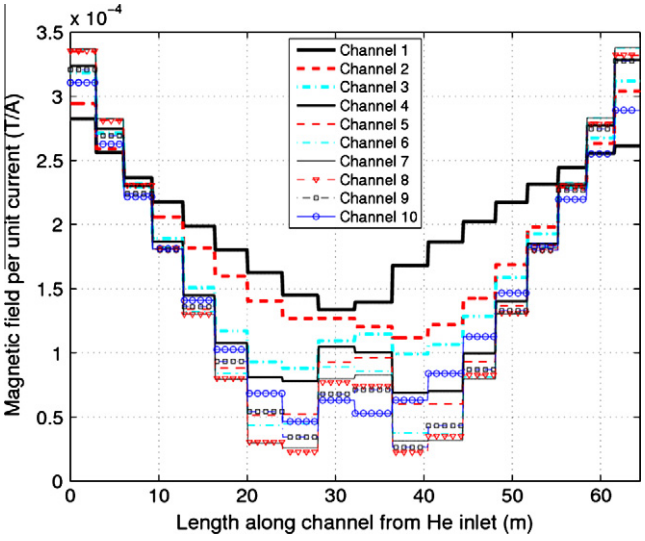

Fig. 5. Magnetic field distribution along each of the 10 hydraulic channels.

pulse time-scale, as already highlighted in [14], because one of the two peak field locations is close to the outlet, on the last turn of each channel. The heating due to the losses on the first turn of each channel is advected to the outlet on a characteristic time comparable to the transit time of the helium in the channels, resulting in a second peak; because of heat diffusion due to the thermal ITIP coupling, the second peak has a smaller amplitude.

In Fig. 6 it is also shown that TCUR03 and TCUR04 present lower amplitude first peaks with respect to TCUR02 and TCUR05. This is a bit surprising, since the magnetic field in the central channels is even higher than in side ones, as already noted. Assuming the TCUR03, 04 behavior is related to some unknown details in the manifold/piping structure (which should in principle be very similar for all outlet pipes), in the next sections we shall concentrate mainly on TCUR02 and TCUR05.

As to the *inlet* temperature, in the shot with the lowest current ramp-down rate only some perturbation of the initial value is detected (Fig. 6a), due to compressibility effects in the circuit during the heating. No backflow is detected in this case, as opposed to what happens in the shot with the highest current ramp-down rate, where the presence of a backflow at the coil inlet is revealed by the inlet temperature increase (Fig. 6b).

3. Simulations

The 4C code [4] has been adopted for the analysis of the KSTAR shots. All 10 channels and their thermal coupling are simultaneously accounted for. The thermal coupling within the coil is modeled starting from a "nominal" configuration based on the series of suitable thermal resistances due to the different layers of turn insulation, see above. The ground insulation and the outer shell (see Fig. 1b) are neglected, as well as the external (radiation/conduction) heat loads, see also [14].

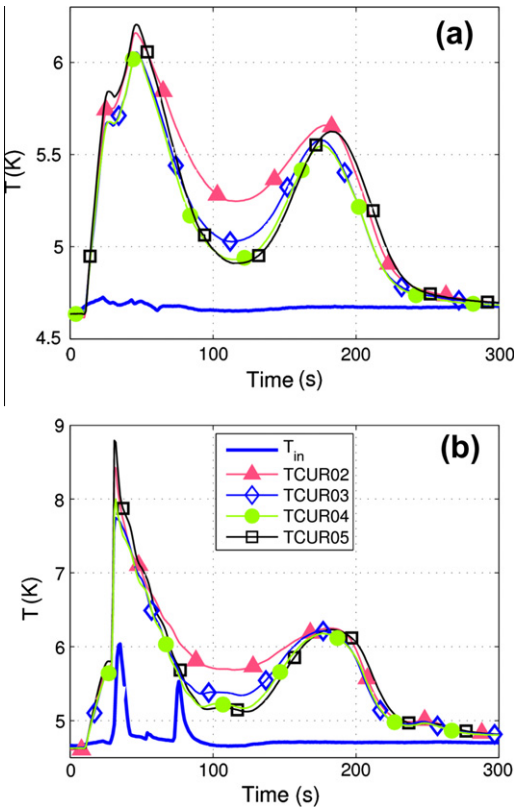

Fig. 6. Thermal–hydraulic effect of the AC losses driven by two different trapezoidal current pulses: (a) slow ramp-down pulse, shot # 4595, and (b) fast ramp-down pulse, shot # 4598. Inlet (thick solid line) and outlet (thin lines with symbols) He temperatures in the PF1L coil.

The AC losses in 4C are implemented using the standard formulas and the parameters reported in [14], except for the $n\tau$ value in the coupling losses, which is discussed below.

3.1. Strategy for AC loss modeling

The analysis of the thermal hydraulic transient induced by the AC losses associated to the trapezoidal current variation is performed adopting the following strategy:

- Couple the model of the coil with a simplified circuit model for the PF1L, based on the actual dimensions of pipes and manifold at coil inlet and outlet, refining the model already presented in [14].
- Calibrate the $n\tau$ in the coupling losses (already shown in [14] to be the dominant contribution to the losses) for each current ramp rate, to find the best fit on the outlet temperatures during the current ramp phase.
- Calibrate the inter-turn/inter-pancake thermal resistance to find the best-fit on the second peak of the outlet temperatures (propagation phase, for which the thermal diffusion through the turn insulation plays a relevant role).
- Compare extensively the computed results with the experimental traces measured not only at outlet but also at the inlet of the coil.

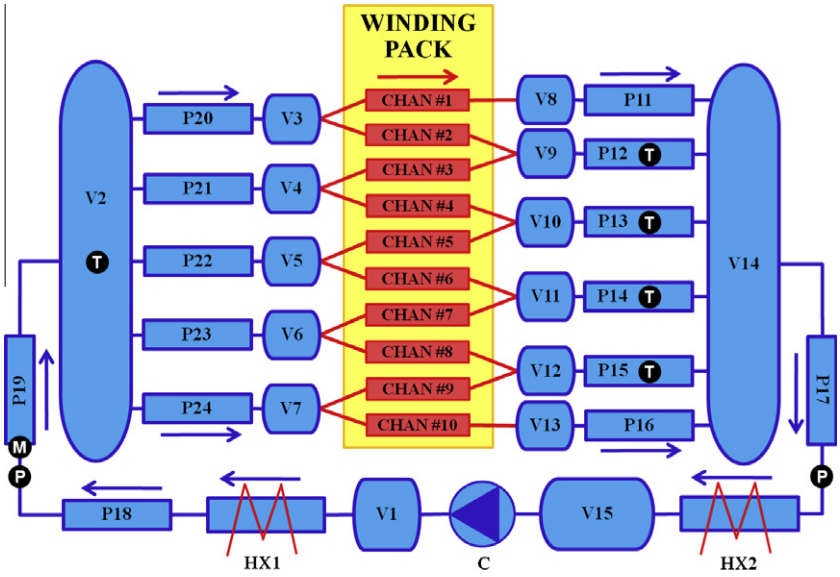

Fig. 7. Schematic view PF1L circuit model. V1-V15 are volumes or manifolds, P11-P24 are pipes, HX1-2 are the heat exchangers, *C* is the circulator, *M*, *P* and *T* are flow meters, pressure and temperature taps, respectively.

Table 2
Main parameters adopted in the circuit model.

Components	Length (m) × diameter (mm)	Volumes	Volume (m^3)
P11	2.735 × 18.038	V1	0.3
P12	1.693 × 18.038	V2	9.98×10^{-3}
P13	1.769 × 18.038	V3	2.245×10^{-4}
P14	1.874 × 18.038	V4	2.338×10^{-4}
P15	1.977 × 18.038	V5	2.443×10^{-4}
P16	2.909 × 18.038	V6	2.578×10^{-4}
P17	5 × 20	V7	2.704×10^{-4}
P18	20 × 20	V8	3.494×10^{-4}
P19	15 × 20	V9	2.162×10^{-4}
P20	1.757 × 18.038	V10	2.260×10^{-4}
P21	1.830 × 18.038	V11	2.394×10^{-4}
P22	1.912 × 18.038	V12	2.525×10^{-4}
P23	2.018 × 18.038	V13	3.716×10^{-4}
P24	2.117 × 18.038	V14	26.78×10^{-3}
HX1	10 × 20	V15	0.35
HX2	10 × 20		
C	dm/dt = 0.0465 kg/s		

3.2. Circuit model

A simplified circuit model has been adopted as shown in Fig. 7. Only the PF1L coil is accounted for, while the other PF coils are not included in the model. While the exclusion of PF1U can be justified by the symmetry assumption, the parallel branches feeding the rest of the PF coils, see Fig. 2, have been neglected only for the sake of simplicity. The size of manifolds and pipes at the coil inlet and outlet correspond to the actual circuit data, while the rest of the circuit is only roughly approximated, in order to guarantee the overall helium inventory in the circuit to be comparable with the experimental one. The values adopted for the circuit model parameters are summarized in Table 2.

We assume for each channel the same friction factor as in [14]; this results in the mass flow rate equally split among channels.

The "virtual" diagnostic location in the circuit model is also represented in Fig. 7, and there the thermal–hydraulic variables computed by 4C will be compared to the corresponding experimental values.

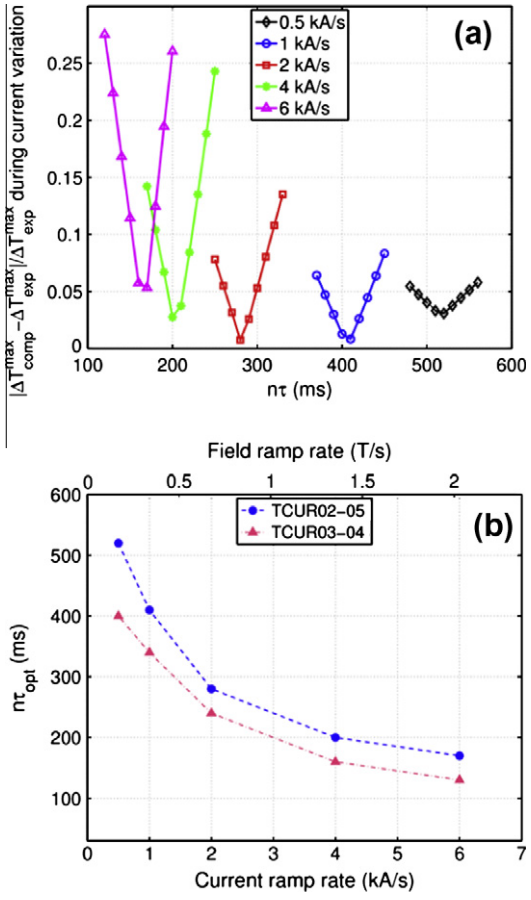

Fig. 8. Results of the calibration study of the $n\tau$ value at different current ramp-rates: (a) absolute value of the relative difference between computed and measured maximum temperature increase during the transient (based on TCUR02 and TCUR05), as a function of the $n\tau$ value assumed in the computation. (b) Optimum value $n\tau_{opt}$ of $n\tau$ as a function of the current ramp rate (lower abscissa) and of the peak field ramp rate (upper abscissa), based on either TCUR02 and TCUR05 or TCUR03 and TCUR04.

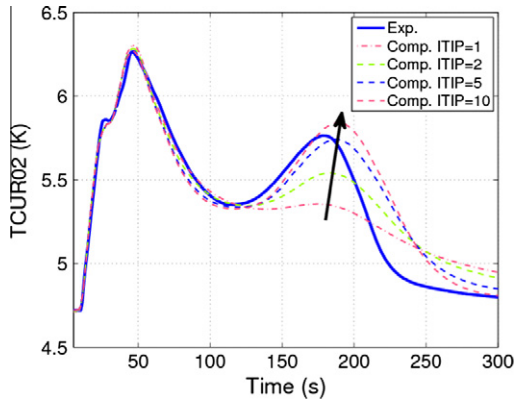

Fig. 9. Calibration of thermal resistance multiplier (ITIP) on the TCUR02 in shot # 4595.

4. Results

4.1. Calibration of $n\tau$ and inter-turn, inter-pancake thermal coupling

For each current ramp rate we determine $n\tau_{opt}$, i.e. the value of $n\tau$ minimizing the difference between computed and experimental maximum temperature increase *during the current variation*:

$$\min\left(\frac{\left|\Delta T^{\max}_{comp}-\Delta T^{\max}_{\exp}\right|}{\Delta T^{\max}_{\exp}}\right). \quad (1)$$

The calibration has been performed first on shot # 4595 on the outlet signals TCUR05 and TCUR02, see above, to get the $n\tau_{opt}$ at 1 kA/s; that has then been frozen for the other shots during the current ramp-up (always at 1 kA/s). Then the value $n\tau_{opt}$ of $n\tau$ best fitting the ramp-down phase at the different current rates has been found. The results of the optimization exercise are reported in Fig. 8a, where at each ramp rate $n\tau_{opt}$ corresponds to the location of the minimum of each curve. As clearly shown in Fig. 8b, $n\tau_{opt}$ decreases progressively for increasing current (and therefore field) ramp rate. This feature was *experimentally* observed in the ITER central solenoid model coil [16]. This behavior was also theoretically explained in [17,18] as related to the presence of several time scales, as opposed to a single one, in multi-stage cables. Based on that, a single $n\tau$ model overestimates the losses for fast transient field changes, since even at moderate dB/dt rates the coupling losses tend to increase less rapidly than single-τ transient formulae would predict [19]. Note also that the $n\tau_{opt}$ found in [14] for the 10 kA/s ramp rate, is in qualitative agreement with this trend. To cross-check the results, the same exercise was repeated based on the outlet signals TCUR03 and TCUR04, and the corresponding $n\tau_{opt}$ at the different ramp rates is also reported in Fig. 8b, showing as expected somewhat lower values than those based on TCUR05 and TCUR02, but the same qualitative behavior.

At all ramp rates considered here, $n\tau_{opt}$ is significantly larger than the values assumed in the conductor design [1], i.e. ~60 ms, as well as than the values from the assessment of the AC losses by applying DC offset sinusoidal currents during the commissioning phase [2], i.e. 30 ms.

The second peak in the outlet temperature, due to the losses in the first turn of each channel as seen above, is strongly influenced by the heat diffusion across the turn insulation. The inter-turn thermal resistance has been calibrated on TCUR02 for shot # 4595 by a suitable multiplier ITIP of the nominal value. In Fig. 9 it is shown that, in the case of a high thermal diffusion (ITIP closer to 1), the second peak is lower (almost vanishing for ITIP = 1) and wider than in the case of a reduced thermal diffusion (larger ITIP), where the peak shrinks to a height comparable to that of the first peak. The best-fitting ITIP value corresponds to an increase of the nominal thermal resistance value by a factor of ~5, which is acceptable considering for instance the contribution of the contact resistances between different insulation layers that are not accounted for in the nominal value. The higher value of the effective thermal resistance of the insulation with respect to the nominal value, needed in order to obtain a good fit between thermal–hydraulic simulation and measured data, was already noted in the past [6,20,21], where a value 6–8 times higher than the nominal one was needed to reproduce the behavior of the Toroidal Field Model Coil during safety discharge tests.

4.2. Comparison with experimental data

The comparison between the 4C results and the measured signals is reported in Fig. 10 (outlet temperatures), in Fig. 11 (inlet/outlet pressures), in Fig. 12 (inlet mass flow rate) and in Fig. 13 (inlet temperature).

As far as the outlet temperature is concerned, the agreement between computation and experiment on the first peak is "guaranteed" by the adoption of $n\tau = n\tau_{opt}$ (different for each shot) in the coupling loss formula, while the agreement on the second peak confirms the proper choice of the ITIP coupling (the same for all shots). However, notice that, besides the peaks, the whole evolution of the output temperature is reproduced with very good accuracy, at least until the second peak. The delay (~10 s over ~150 s) in the second peak is within the accuracy of the friction factor derived in [14].

The computed pressure rise in the circuit, both at the coil inlet and outlet, shows a reasonable agreement with the experiment in the current ramp-up and ramp-down phases, see Fig. 11, while the subsequent evolution back to the initial values follows in the simulations a quite different path with respect to the experimental

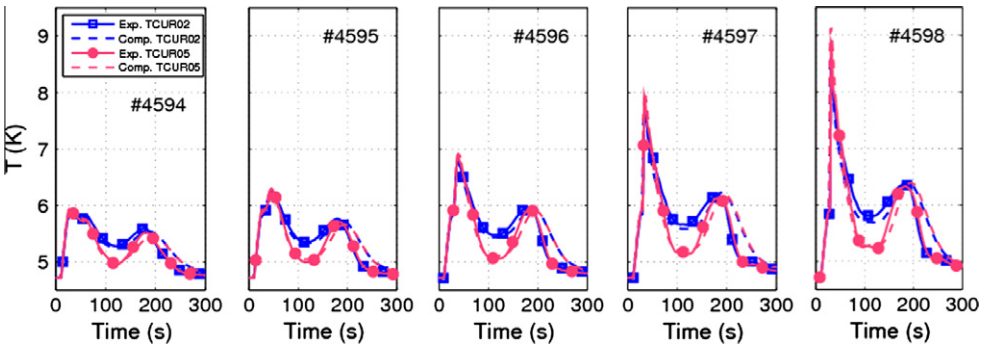

Fig. 10. Computed (dashed lines) vs. measured (solid lines with symbols) outlet He temperature evolution for all shots.

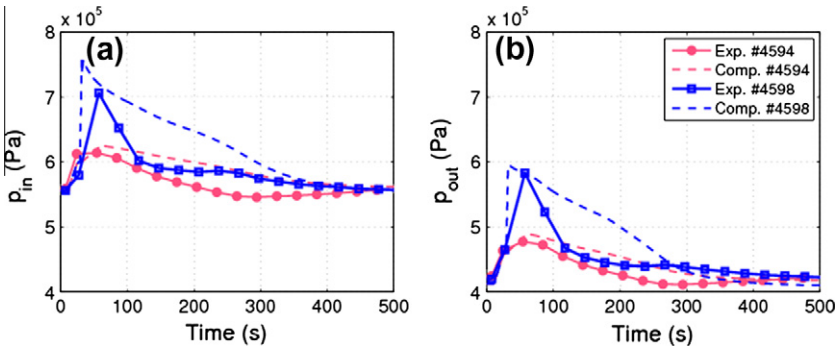

Fig. 11. Computed (lines) vs. measured (symbols) He pressure evolution at the coil inlet (a) and outlet (b), for the slowest and fastest ramp rates.

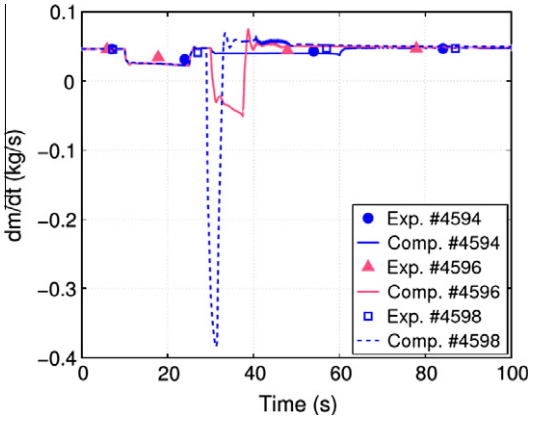

Fig. 12. Computed (lines) and experimental (symbols) helium mass flow rate evolution at the coil inlet for three shots with no backflow, intermediate backflow and strong backflow, respectively.

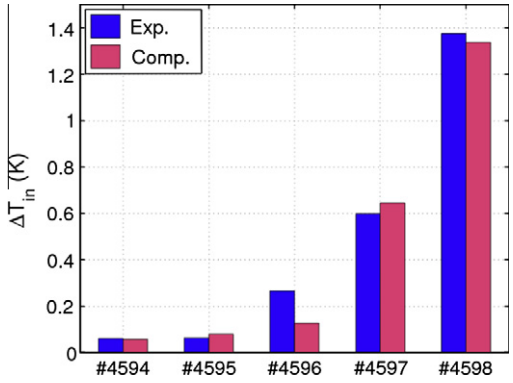

Fig. 13. Computed vs. measured maximum temperature increase at the coil inlet for the different shots.

data. This could be an effect of the simplified circuit model adopted here, which does not account for all the hydraulic paths in parallel to the PF1L, see Fig. 2.

The computed inlet mass flow rate shows no backflow in the simulations for the shots at the lowest ramp rates (up to 1 kA/s), while it shows a progressively stronger backflow at current ramp-down rates $\geqslant$ 2 kA/s, see Fig. 12. Although it is not possible to confirm this only by looking at the experimental mass flow rate signal, in view of the fact that an orifice is used for the measurement and the data acquisition rate is very low, this is clearly in qualitative agreement with the measured inlet temperature signal, which may show a noticeable increase (>0.1 K) only in the presence of backflow.

Also the values of the computed maximum inlet temperature increase agree well with the measured values, see Fig. 13, for all shots considered here, confirming that our simulations reproduce all the main features of the experimental results with good accuracy.

5. Conclusions and perspective

A complete set of trapezoidal current scenarios with different ramp-down rates in the KSTAR PF1 coils has been analyzed with the 4C code.

The coupling time constant $n\tau$ was calibrated at the different ramp rates, based on the value of the maximum measured He temperature at the coil outlet, leading to a decreasing trend of this optimum $n\tau$ as the ramp rate increases, which is well known in the literature. At any ramp rate the optimum $n\tau$ is however much larger than the design value.

The inter-turn/inter-pancake thermal coupling was calibrated based on the second peak of the measured He temperature at the coil outlet, which is justified in view of the multi-layer nature of the (electrical) turn insulation, introducing a contact resistance.

A very good agreement between the computed and the measured signals was shown, not only at the coil outlet, which is partly a result of the calibration, but also at the inlet, showing the full adequacy of the 4C code, within the limitations of the presently adopted simplified circuit model.

In perspective we plan to develop a comprehensive thermal–hydraulic model of the entire PF magnet system in KSTAR and we believe that, based on the present very encouraging results, the 4C code can become a useful tool for the thermal–hydraulic analysis and for the design of future operating scenarios of the KSTAR superconducting magnet system.

References

[1] Oh YK et al. Commissioning and initial operation of KSTAR superconducting tokamak. Fus Eng Des 2009;84:344–50.
[2] Lee HJ et al. The AC loss measurement of the KSTAR PF1 coils during the first commissioning. IEEE Trans Appl Supercond 2010;20:551–5.
[3] Park YM et al. Analysis of the helium behavior due to AC losses in the KSTAR superconducting coils. IEEE Trans Appl Supercond 2010;20:530–3.
[4] Savoldi Richard L, Casella F, Fiori B, Zanino R. The 4C code for the cryogenic circuit conductor and coil modeling in ITER. Cryogenics 2010;50:167–76.
[5] Bonifetto R, Kholia A, Renard B, Rie K, Savoldi Richard L, Zanino R. Modeling of W7-X superconducting coil cool-down using the 4C code. Fus Eng Des 2011;86:1549–52.
[6] Zanino R, Bonifetto R, Heller R, Savoldi Richard L. Validation of the 4C thermal–hydraulic code against 25 kA safety discharge in the ITER toroidal field model coil (TFMC). IEEE Trans Appl Supercond 2011;21:1948–62.
[7] Savoldi Richard L, Bonifetto R, Heller R, Zanino R. Thermal–hydraulic Simulation of 80 kA safety discharge in the ITER toroidal field model coil (TFMC) using the 4C code. IEEE Trans Plasma Sci 2012;40:782–7.

[8] Bonifetto R, Casella F, Savoldi Richard L, Zanino R. Dynamic modeling of a SHe closed loop with the 4C code. Adv Cryo Eng, in press.
[9] Bonifetto R, Casella F, Savoldi Richard L, Zanino R. Validation of the 4C code cryogenic circuit model against data from the Helios/JT60SA loop at CEA Grenoble. Cryogenics; in press.
[10] Bonifetto R, Domalapally PK, Polli GM, Savoldi Richard L, Turtu' S, Villari R, et al. Computation of JT-60SA TF coil temperature margin using the 4C code. Fus Eng Des 2011;86:1493–6.
[11] Bonifetto R, Buonora F, Savoldi Richard L, Zanino R. 4C code simulation and benchmark of ITER TF magnet cool-down from 300 K to 80 K. IEEE Trans Appl Supercond; in press. doi:http://dx.doi.org/10.1109/TASC.2011.2177233.
[12] Zanino R, Bessette D, Savoldi Richard L. Quench analysis of an ITER TF coil. Fus Eng Des 2010;85:752–60.
[13] Savoldi Richard L, Bonifetto R, Bessette D, Zanino R. Parametric analysis of the ITER TF fast discharge using the 4C code. IEEE Trans Appl Supercond; in press. doi:http://dx.doi.org/10.1109/TASC.2012.2188130.
[14] Zanino R, Chu Y, Kholia A, Lee HJ, Park SH, Savoldi Richard L. Simulation of thermal–hydraulic transients in the KSTAR PF1 coil using the 4C code. IEEE Trans Plasma Sci 2012;40:710–4.
[15] Park SH et al. Thermohydraulic behavior of KSTAR PF superconducting magnet system in operation. IEEE Trans Appl Supercond; in press. doi:http://dx.doi.org/10.1109/TASC.2011.2175890.
[16] Martovetsky N, Michael P, Minervini J, Radovinsky A, Takayasu M, Gung CY, et al. Test of the ITER central solenoid model coil and CS insert. IEEE Trans Appl Supercond 2002;12:600–5.
[17] Bruzzone P, Fuchs AM, Vecsey G, Zapretilina E. Test results for the high field conductor of the ITER central solenoid model coil. Adv Cryo Eng 2000;45:729–36.
[18] Nijhuis A, Ten Kate HHJ, Duchateau JL, Bruzzone P. Coupling loss time constants in full-size Nb_3Sn CIC model conductors for fusion magnets. Adv Cryo Eng 1996;42:1281–8.
[19] ITER. Magnet superconducting and electrical design criteria. Annex to design requirements and guidelines level 1 (DRG1). N 11 MA 2 04–04-27 R 0.1.
[20] Ulbricht A et al. The ITER toroidal field model coil project. Fus Eng Des 2005;73:189–327.
[21] Duchateau JL et al. ITER toroidal field model coil test: analysis of heat transfer from plates to conductors. Fus Eng Des 2003;66–68:1007–11.